## 4.1 INTRODUCTION

Numerous Bragg grating manufacturing techniques have been developed since the first Bragg grating by Hill *et al*. in 1978. [1] A review of the most dominant methods is presented with a brief look at photosensitivity of optical fibres and Bragg grating annealing. Practical OADMs using Bragg gratings need high-channel isolation Bragg gratings. A theoretical design and experimental results of high-channel isolation Bragg gratings is presented.

Bragg gratings are extremely susceptible to fluctuations in ambient temperatures. Ideally one would like the Bragg grating to be stable over a wide range of temperatures for OADMs. By using special packaging methods, one can counteract the shift in central wavelength of Bragg gratings due to temperature drifts. A theoretical design and experimental results are presented regarding athermal Bragg gratings. We conclude with experimental results regarding a three-port circulator and Bragg grating OADM.

## 4.2 MANUFACTURING FIBRE BRAGG GRATINGS

### 4.2.1 Photosensitivity of optical fibres

Photosensitivity of optical fibres is an abstract phenomenon for which many hypotheses have been proposed to explain the mechanics behind the process. Hill *et al.* first discovered the phenomenon, while conducting experiments on nonlinear effects in silica optical fibres. [1] Hill and his team launched visible blue light at *488 nm* from a single-mode argon laser through a beam splitter into a germanium-doped silica single-mode optical fibre. The weak standing wave pattern resulting from interference between the launched light and the counter-propagating Fresnel-reflected light exposed the core of the optical fibre to form a permanently inscribed refractive index grating with a period equal to that of the interference pattern. The intensity of the reflected light grew stronger over time. They called the phenomenon fibre photosensitivity. [1]

The most eminent model, proposed by Meltz, explains the process in terms of oxygen vacancy defects in the glass lattice. [1] Germanium-doped silica fiber has a strong absorption peak at *248 nm*. When this absorption band is bleached with UV light, other UV and visible absorption bands are created. The change in absorption results in a refractive index change through the Kramers-Kronig causality relationship. [1]

High-quality fibres contain low concentrations of defects. Therefore, defects have to be created in the core, which are strongly absorbing at the activating wavelength, and that are of the type that lead to photosensitivity. Hydrogen flame brushing and high-pressure hydrogen loading are two techniques used for photosensitization of Germanium-doped silica fibres. [2] Hydrogen molecules diffuse into the core and, when exposed to UV light, will react at the Ge sites in the $GeO_2$-doped fibre resulting in an increase of the refractive index of the core. Through the use of hydrogen loading a refractive index change as high as $10^{-2}$ has been obtained. [2]

An alternative model based on glass densification induced by photoionization of the GeO defects has also been proposed. [3] Increased photosensitivity has been achieved by codoping the core with $B_2O_3$ and $GeO_2$. Boron causes stress-induced refractive index changes in silica-based fibres. This mechanism therefore supports the idea that densification makes an important contribution to the photoinduced changes. [3] A variety of dopants, such as Germanium, Boron, Tin and rare earth ions, can be used to increase the photosensitivity of fibres. [2]

The UV-source wavelength also plays an important role in determining the amount of induced index that can be achieved. The most commonly used light sources are KrF (*248 nm*) and ArF (*193 nm*) excimer lasers. The fibre is typically exposed for a few minutes at intensities ranging from *100* to *1000 mJ/cm*$^2$ with a pulse repetition of *50 - 75 Hz*. Irradiation at intensity levels higher than *1000 mJ/cm*$^2$ causes a nonlinear photosensitive process that enables a single irradiating excimer light pulse to produce large index changes in a small localized region near the core/cladding boundary. [4]

It is likely that more than one mechanism is involved in photosensitivity of optical fibres and that the relative influence of each is dependent on the parameters of the

specific fibre type, the photosensitization procedure and the writing process (laser power and wavelength). [3]

### 4.2.2 Manufacturing methods for fibre Bragg gratings

The original fibre Bragg gratings or Hill gratings, as they are known, were produced by writing a refractive index grating internally in the core of the optical fibre. The original experimental setup is shown in Figure 4.1. [1]

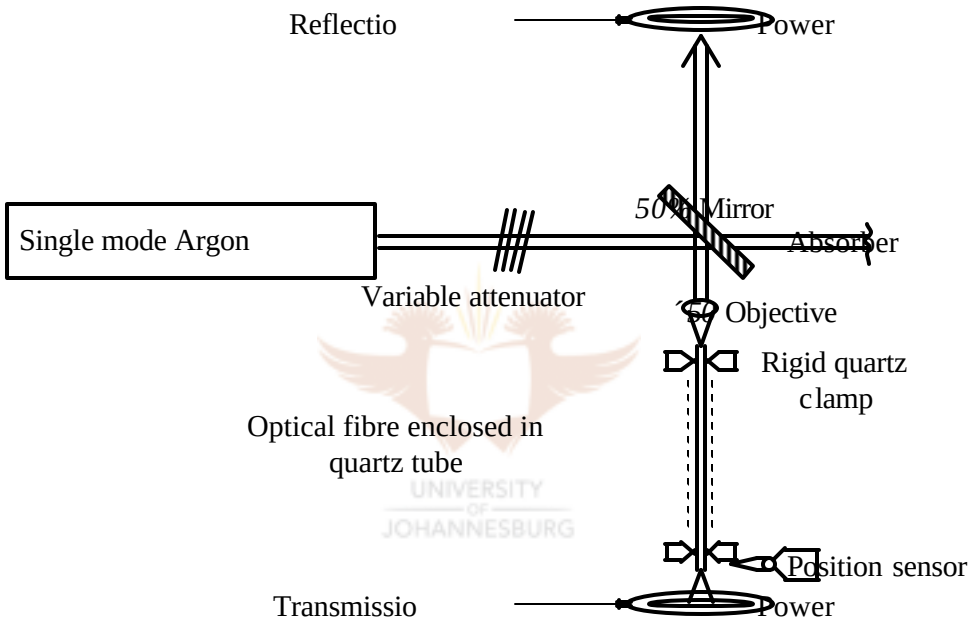


**Figure 4.1 - Original experimental setup for writing "Hill" gratings [1]**

Visible blue light at 488 nm from a single-mode argon laser is launched through a beam splitter into a Germanium-doped silica single-mode optical fibre. The weak standing wave pattern resulting from interference between the launched light and the counter-propagating Fresnel-reflected light exposes the core of the photosensitive optical fibre to form a permanently inscribed refractive index grating with a period equal to that of the interference pattern. The intensity of the reflected light due to the weak index grating is small in the beginning but as the grating becomes stronger, more light is coupled to such an extent that a saturation point of *100 %* reflected light

can be ascertained. Hill produced a *1 m* long grating with a refractive index change in the order of $10^{-5}$ to $10^{-6}$, a maximum reflection of *88 %* and an FWHM of *200 MHz*. [1], [5]

The original internal writing technique had quite a few limitations that slowed the advancement of Bragg gratings to be used as filters in fibre optic communication systems. The repeatability of the experiment was difficult to achieve and it was thought that the phenomenon was confined to the one "magical" fibre at CRC. Another major problem was that the writing wavelength determined the operating wavelength of the reflection grating. Only filters in the blue-green visible spectrum (*488 nm* and *514.5 nm*) have been written, whereas the spectrum for fibre optic communications ranged in the near infrared region from about *700 nm* to *1600 nm*. [1]

More than a decade later, Meltz *et al.* announced the first practical solution to produce Bragg gratings. Theirs was a transverse two-beam holographic method using single-photon absorption at *244 nm* in externally writing a Bragg grating in the Germanium-doped core of the fibre. [6] The Bragg grating reflected light in the visible wavelength region *577 nm* to *591 nm*. The knowledgeable choice of the UV writing wavelength was based on work done by Lam and Garside. [7] They showed that the grating strength depends on the square of the light intensity. Deriving from the energy of a photon given by:

$$E = \frac{hc}{l} \tag{4.1}$$

where $h = 6.63 \times 10^{-34}$ *J.s* is Planck's constant and $l$ is the writing wavelength. They showed that photosensitivity at *488 nm* was a two-photon process and only a one-photon process at *244 nm.* Meltz achieved a *4.4 mm* Bragg grating with a refractive index change of $3 \times 10^{-5}$, a maximum reflection of *55 %* and an FWHM of *42 GHz*. [6] Figure 4.2 shows a typical transverse holographic configuration for writing index gratings in the core of optical fibres by externally irradiating the fibres. This method made the index grating manufacturing far more versatile and practical.

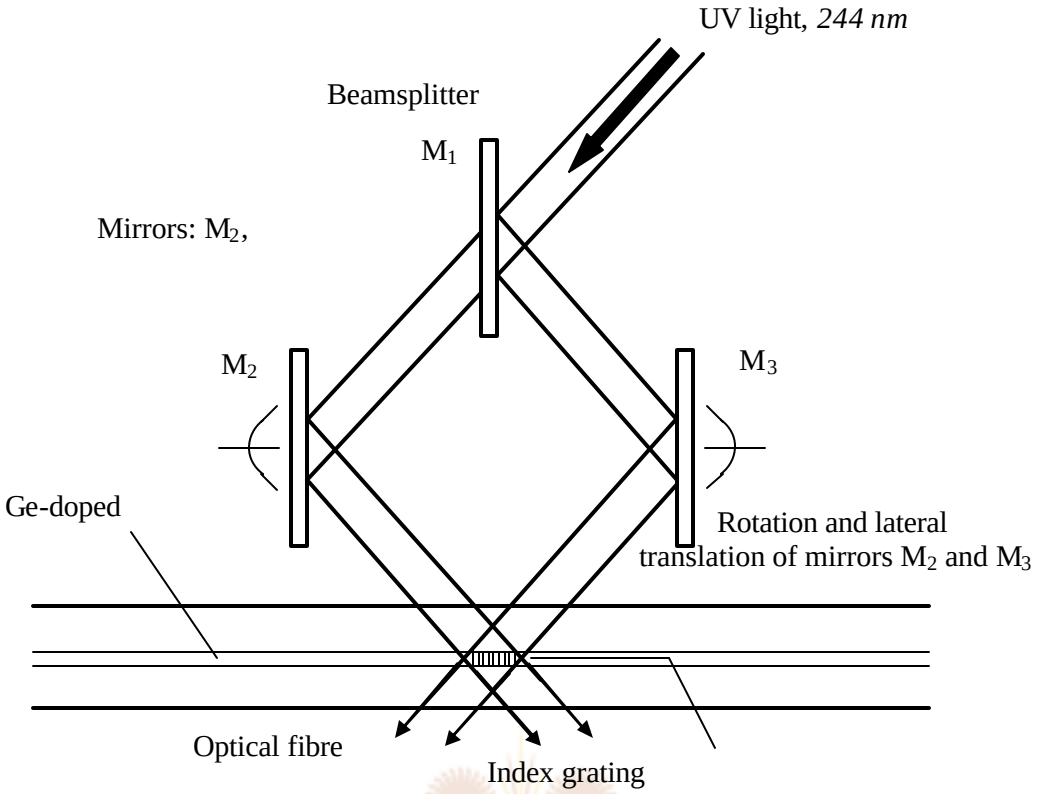


**Figure 4.2– Transverse two-beam holographic method for writing index gratings externally in the core of a Ge -doped core fibre [1]**

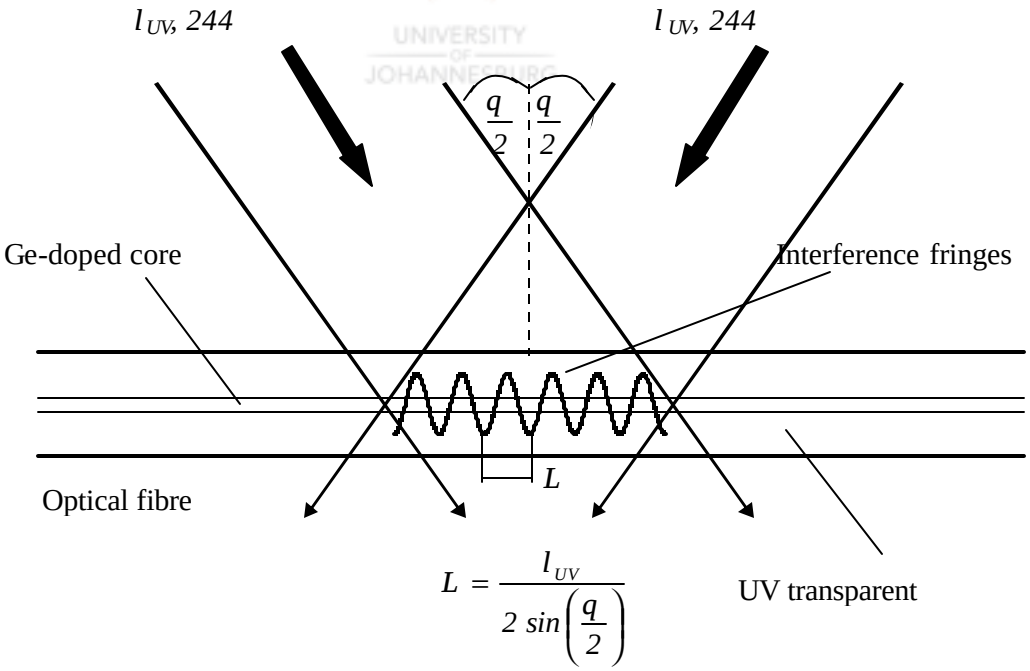


**Figure 4.3 – A magnified look at the formation of interference fringes during the inscription of a Bragg grating by two interfering UV beams [3]**

A closer look at the fringes in Figure 4.3 reveals that the period of the index grating is not only dependent on the writing wavelength but also on the angle $q$ between the two interfering light beams. Therefore, through the rotational and lateral translation of the mirrors in Figure 4.2, one can obtain custom Bragg gratings at functional wavelengths for fibre optic communications. [(1), (3)]

A popular technique for writing gratings involves "contact printing" through a phase mask. The phase mask is itself a grating, etched in a silica substrate, with an etching depth such that it diffracts most of the light in the $+1$ and $-1$ orders. [(3)] These diffraction orders generate the interference pattern. The phase mask is designed to suppress the diffraction into the zero-order by controlling the depth of the corrugations of the phase mask. In practice, the amount of light in the zero order can be reduced to less than $5\ \%$ with approximately $40\ \%$ of the total light intensity divided equally between the $+1$ and $-1$ orders. [(8)]

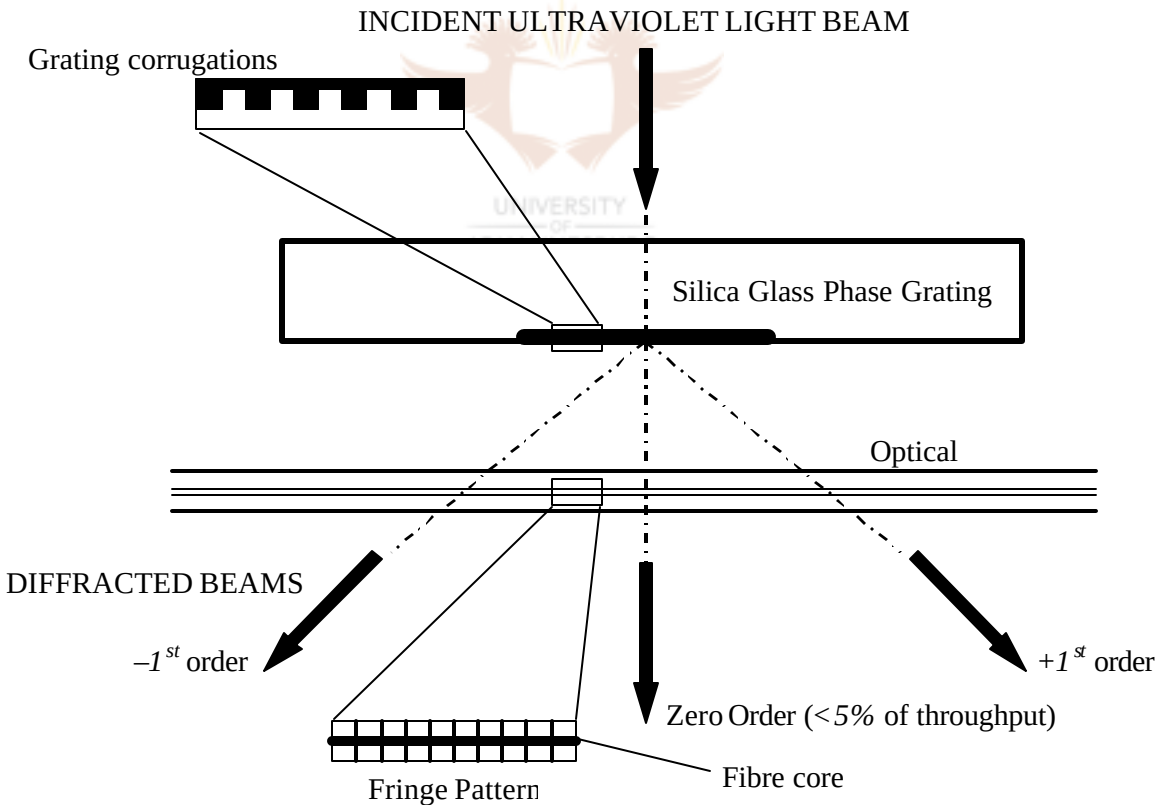


**Figure 4.4 – Bragg grating inscription by UV exposure through a phase mask [(8)]**

The fibre is placed directly behind the mask and exposed either to a beam having a width corresponding to the desired grating length or to a narrower beam that is translated back and forth along the mask. The latter method is preferred because it makes the grating shape independent of the beam shape or width and allows the grating strength to be varied at will along the grating to generate a particular profile. [8]

If the period of the phase mask grating is $L_{mask}$, then the period of the UV-induced grating would be $L_{mask}/2$. This period is independent of the UV source irradiating the fibre. [4] The phase mask method is much simpler than the methods mentioned previously and offers easier alignment of the fibre for photoimprinting, reduced stability requirements on the photoimprinting apparatus and power coherence requirements on the UV-laser source. A drawback of the phase mask method is that the gain in simplicity increases the loss in flexibility. A separate phase mask is required for each different Bragg wavelength. There are however methods to change the period of the grating using lenses and by stretching the fibre before exposure. [4]

### 4.2.3 Bragg grating annealing



Practical OADMs are intended for use over a long period ($> 25\ years$). A Bragg grating must therefore have a long service life. In Bragg gratings written through hydrogen loading, any unreacted hydrogen remaining when UV exposure is completed diffuses back out of the fibre. The presence of dissolved, unreacted hydrogen temporarily increases the fibre refractive index, and its subsequent, slow diffusion leads to a shift in the centre Bragg wavelength. [3] By accelerating ageing tests, it has been shown that a post-exposure annealing step can effectively stabilize the properties of Bragg gratings against any long-term variations due to hydrogen diffusing and induced-index degradation. [9]

The annealing process involves exposing the Bragg grating to elevated temperatures ($> 85\ ^{\circ}C$) for a short period in order to diffuse the hydrogen and erase the unstable part of the UV-induced index change that would decay over the lifetime of the device. [9]

## 4.3 HIGH-CHANNEL ISOLATION BRAGG GRATINGS

### 4.3.1 Theoretical design

In section 3.3.3, *apodization* of the grating profile was discussed. It was shown that through *apodization*, the sidelobes could be suppressed to realize Bragg gratings exhibiting high-channel isolations. Different *apodization* profiles (or windowing functions) can be used to optimize the suppression of the sidelobes. The main *apodization* profiles considered in this investigation include:

- the Hamming profile
- the Blackman profile
- the sinc profile
- the Gaussian profile, and
- the Kaiser profile.

Hamming and Blackman are members of the *cosine* series windows, where the window coefficients are given by: [10]

$$w(z) = \sum_{l=0}^{K} a_l \cos\left[\frac{2\pi l}{L}\left(z - \frac{L}{2}\right)\right], \quad 0 \le z \le L \tag{4.2}$$

where $L$ is the window length. The Hamming window requires $a_0 = 0.42$ and $a_1 = 0.50$ whereas the Blackman window requires an additional coefficient $a_2 = 0.08$. Optimization of these coefficients leads to the minimization of the maximum sidelobe levels.

The *sinc* profile is given by: [11]

$$w(z) = \frac{\sin(x)}{x}, \quad x = \frac{2\pi\left(z - \frac{L}{2}\right)}{L}, \quad 0 \le z \le L \tag{4.3}$$

The Gaussian profile is given by: [12]

$$w(z) = exp\left[\frac{-\left(z-\frac{L}{2}\right)^2}{2s_z^2}\right], \quad 0 \le z \le L \tag{4.4}$$

The Gaussian function is spread around the peak midpoint ($L/2$) with the spreading related to $s_z$. The function decreases to $0.607$ times its maximum at $z = L/2 + s_z$ and $z = L/2 - s_z$.

The Kaiser window of length $L$ is based on the modified Bessel function $I_0(x)$: [10]

$$w(z) = \frac{I_0\left(b\sqrt{1-\left(z-\frac{L}{2}\right)^2 \Big/ \left(\frac{L}{2}\right)^2}\right)}{I_0(b)}, \quad 0 \le z \le L \tag{4.4}$$

The parameter $b$ offers a trade-off between the sidelobe height and the width of the mainlobe, and should be chosen between $0$ and $10$, for useful windows.

The various envelopes of the peak-to-peak index modulation of different DC-*apodization* profiles are plotted in Figure 4.5 for visualization and comparison. Figure 4.6 and Figure 4.7 show the calculated reflectivity for a $10\ mm$ grating, with $n_{co} = 1.46, Dn(z) = 3 \times 10^{-4}$ and *apodized* with the different *apodization* profiles.

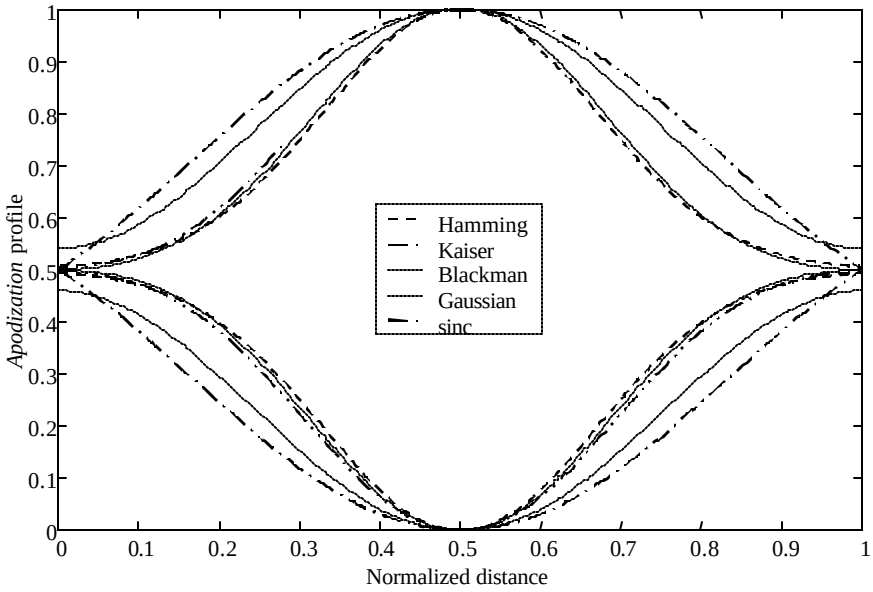


**Figure 4.5 – Various DC-apodization profiles**

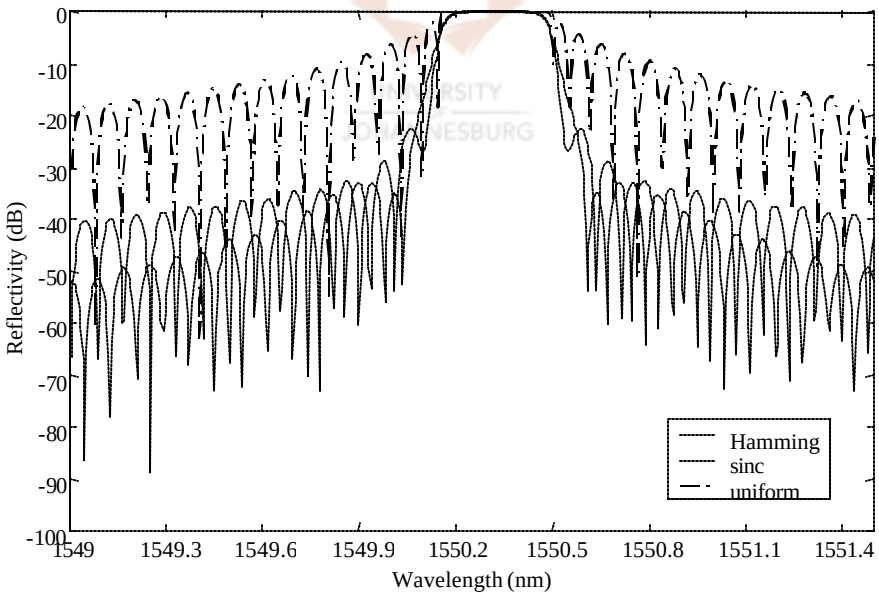


**Figure 4.6 – Reflectivity of a Hamming, sinc and uniform grating**

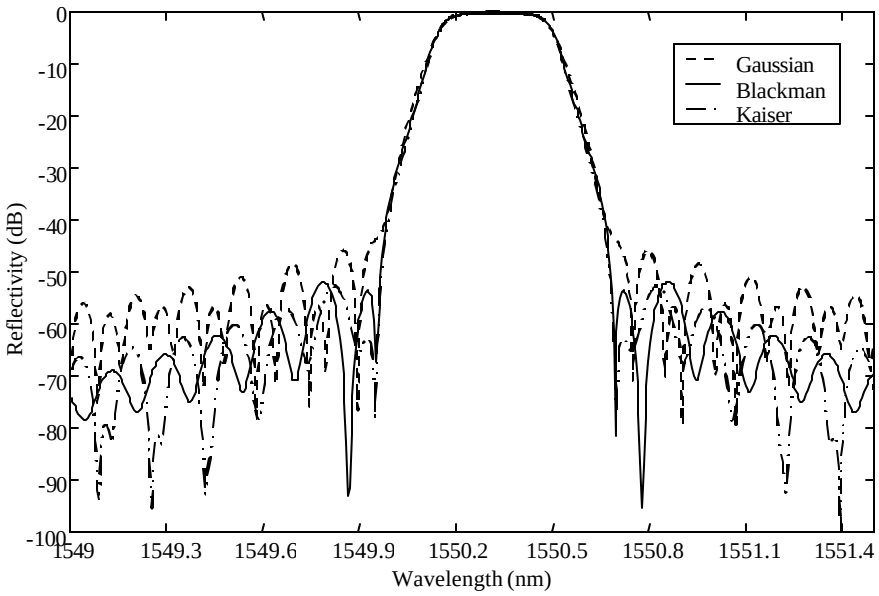


**Figure 4.7 – Reflectivity of a Gaussian, Blackman and Kaiser grating**

The *apodization* parameters regarding each type of window considered in this analysis are listed in Table 4.1. It is evident from Figure 4.6 and Figure 4.7 that the Gaussian, Blackman and Kaiser DC-*apodization* profiles result in the best suppression of the sidelobes. By optimizing the relevant parameters for each type of window, one can even reduce the sidelobes further and therefore optimize the performance of each filter.

| ***Apodization* profile** | **Parameters** |
|---|---|
| Hamming | $a_0 = 0.42,\ a_1 = 0.50$ |
| Blackman | $a_0 = 0.42,\ a_1 = 0.50, a_2 = 0.08$ |
| Gaussian | $s_z = L/6$ |
| Kaiser | $b = 8$ |

**Table 4.1 – Coefficients used for the different *apodization* profiles**

We selected the Gaussian and Kaiser *apodization* profiles to design two *15 mm* DC-*apodized* gratings. We will refer to these gratings as Grating 1 and Grating 2

respectively. Grating 1 has an ac index change of $Dn(z) = 2\acute{}10^{-4}$ and Grating 2, $Dn(z) = 3\acute{}10^{-4}$ ($n_{co} = 1.46$ for each grating). Figure 4.8 shows the reflectivity of these gratings respectively.

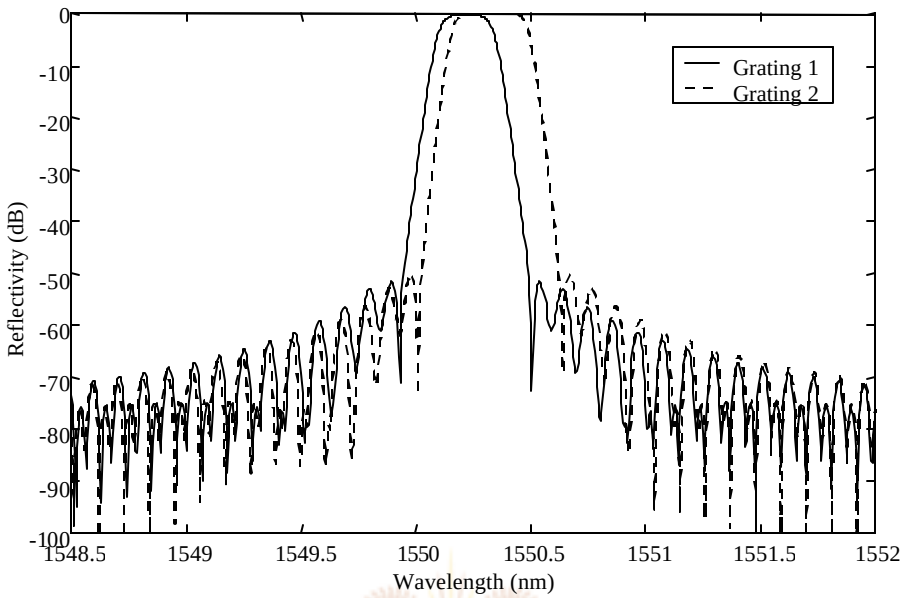


**Figure 4.8 – Reflectivity of Grating 1 (Gaussian, $Dn(z) = 2\acute{}10^{-4}$) and Grating 2 (Kaiser $Dn(z) = 3\acute{}10^{-4}$)**



Grating 1 exhibits an FWHM of *0.227 nm* and a channel isolation of *51.67 dB* whereas Grating 2 has an FWHM of *0.324 nm* and a channel isolation of *50.08 dB*.

### 4.3.2 Experimental results

To realize DC-*apodized* gratings practically, one must precondition the core of the fibre to equalize the effect of the UV-written Bragg grating. Without preconditioning, the result will be a grating with an effective index changing over the length of the grating as shown in Figure 3.13. The preconditioning can be done by either a shadow mask or by simply translating the UV beam (without the phase mask) across the desired grating length to raise the index to the appropriate level. [13]

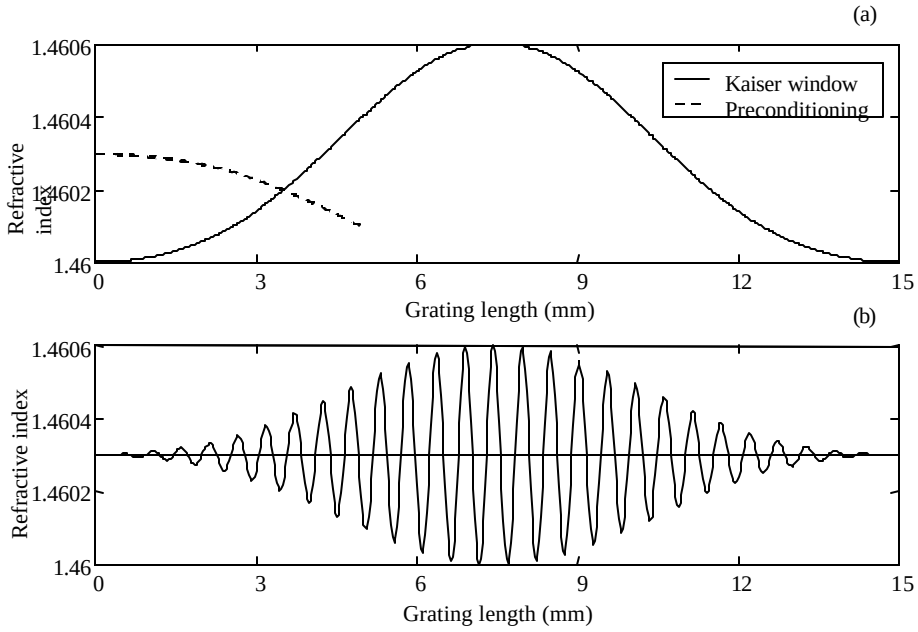


**Figure 4.9 – Writing process for Grating 2, with (a) being the preconditioning and the Kaiser window and (b) the resultant peak-to-peak index modulation**

Figure 4.9 (a) shows simulated graphs of the preconditioning and the Kaiser window for Grating 2. Figure 4.9 (b) shows the peak-to-peak index modulation and effective index for the end result of the individual processes. The period of the grating has been greatly exaggerated for illustrative purposes. It is important to notice that the effective index in Figure 4.9 (b) remains constant over the entire length of the grating. Any change in the effective index will result in an asymmetrical reflection spectrum.

Figure 4.10 and Figure 4.11 show experimental reflection spectra for Grating 1 and Grating 2. The two Bragg gratings were UV written by using a KrF (*248 nm*) excimer laser in the core of a Boron-doped PS-1550 photosensitive fibre. Grating 1 was prestrained by *150 me* and Grating 2 by *200 me*, resulting in a shift of *1.87 nm* and *2.54 nm* after relaxing the fibres respectively. Grating 1 exhibits a peak reflectance of *50.69 %*, an FWHM of *0.183 nm* and a channel isolation of *22.17 dB*, whereas Grating 2 has a peak reflectance of *77.9 %*, an FWHM of *0.201 nm* and a channel isolation of *24.61 dB*.

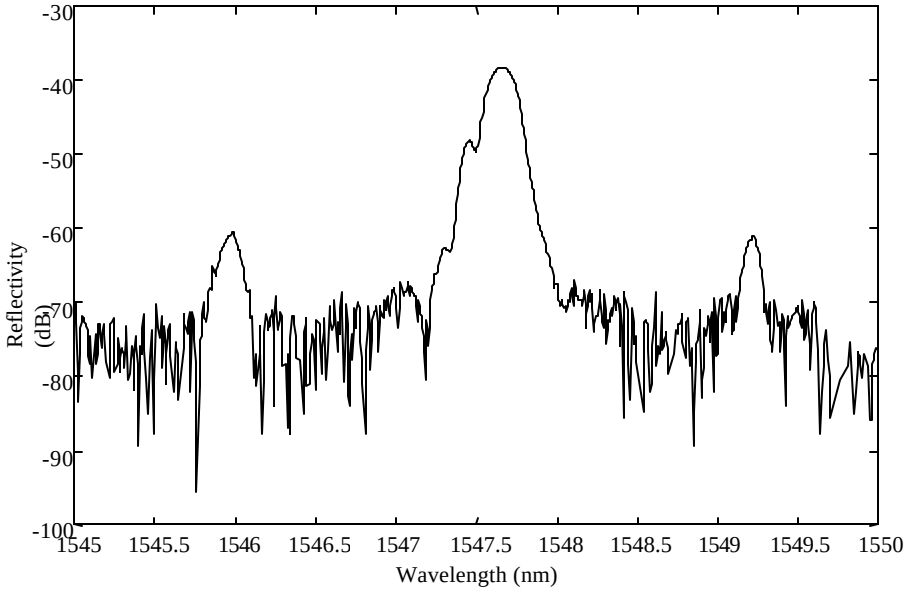


**Figure 4.10 – Experimental reflectivity for Grating 1 (Gaussian, $Dn(z) = 2 \times 10^{-4}$)**

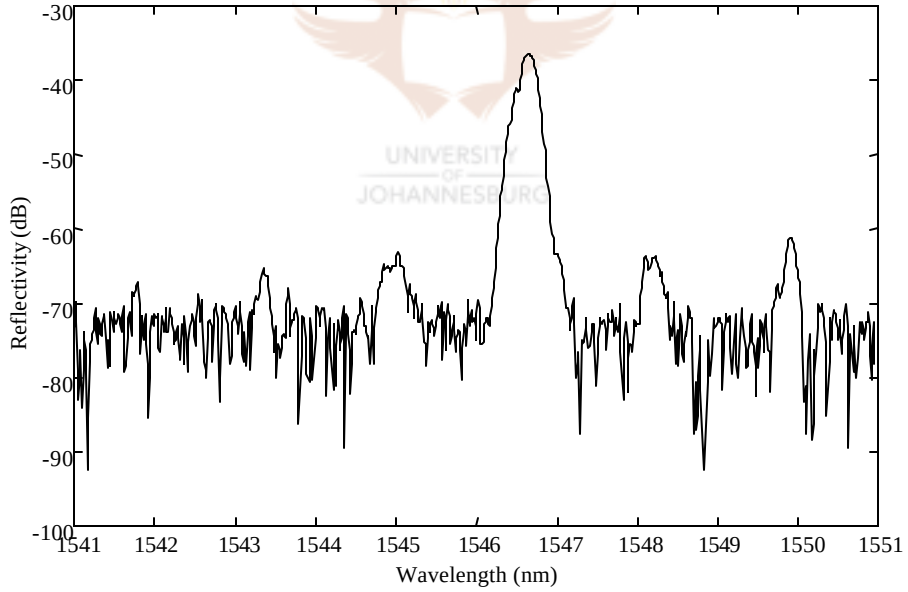


**Figure 4.11 – Experimental reflectivity for Grating 2 (Kaiser, $Dn(z) = 3 \times 10^{-4}$)**

The low reflectance and smaller spectral widths are due to a lower-than-designed induced index change caused by the writing procedure. The theoretical values are

ideal simulations and do not take into account external factors that may influence the performance of the inscribed Bragg grating. The amount of irradiation dosage that is needed for a specific induced index change depends on:

- UV-source wavelength and power
- Fibre type
- Type of photosensitization
- Fibre temperature

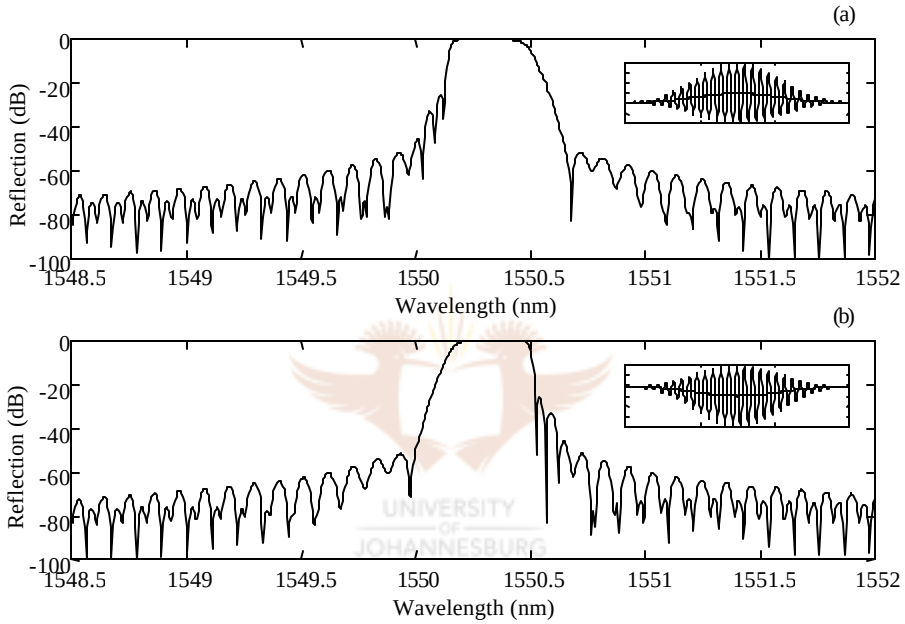


**Figure 4.12 – Simulated reflectance of Grating 2 with (a) 30 % under-preconditioning and (b) 30 % over-preconditioning**

The asymmetrical reflection spectra (Figure 4.10 and Figure 4.11) are due to under-preconditioning causing the effective index to vary over the length of the grating. Figure 4.12 (a) and Figure 4.12 (b) show simulated effects when the preconditioning is not enough (under-preconditioned by *30 %*) and too much (over-preconditioned by *30 %*) for Grating 2. The insets are schematic representations of the grating peak-to-peak index modulation and average index modulation. The period of the grating has been greatly exaggerated for illustrative purposes. The reason for the reflectance of

the shorter and the longer wavelengths in each case originate from Fabry-Perot resonance. The wings of the grating act like a Fabry-Perot cavity at the shorter and longer wavelengths respectively. The associated wavelengths therefore experience a strong reflection at the wings. [14]

A strange phenomenon to notice in Figure 4.10 and Figure 4.11 is the sidelobes that are situated far from the mainlobe. This is due to a modulation in the envelope of the grating profile and occurs during the UV-writing process. The gratings were written with a phase mask. The UV beam (*2 mm* in width) was moved with increments of *500 mm* along the entire length of the grating. The modulation is "stitching" errors resulting in an envelope that is not smooth, but a staircase type of envelope. Figure 4.13 shows a simulation of Grating 2, which is 30 % under-preconditioned, with "stitching" errors. The period of the envelope modulation is *500 mm*. The simulated sidelobe phenomenon compares fairly well with the experimental results obtained. The width between the simulated sidelobes is ± *1.1 nm* whereas for the experimental sidelobes, it is ± *1.6 nm*. Ignoring the "stitching" errors, a channel isolation of *29 dB* for Grating 1 (spectrum: *1546.25 nm* to *1549.2 nm*) and *34 dB* for Grating 2 (spectrum: *1545.3 nm* to *1548 nm*) are expected.

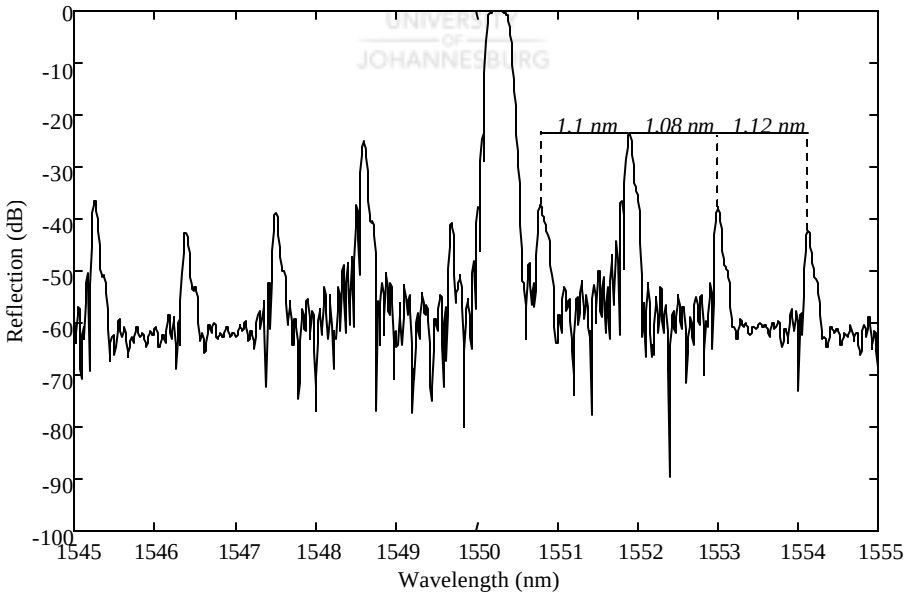


**Figure 4.13 – Simulated reflectivity for Grating 2 (Kaiser, $Dn(z) = 3 \times 10^{-4}$) with a modulated envelope**

## 4.4 ATHERMAL BRAGG GRATINGS

Bragg gratings are extremely susceptible to fluctuations in ambient temperatures. Ideally, one would like the Bragg grating to be stable over a wide range of temperatures for OADMs. By using special packaging methods, one can counteract the shift in the central wavelength of the Bragg gratings due to temperature drifts.

The temperature-compensating package normally comprises two materials exhibiting different thermal expansion coefficients or alternatively only one material with a negative thermal expansion coefficient. In both methods, the fibre Bragg grating is mounted under tension on the relevant materials. [15]

A possible option for the extraordinarily negative thermal expansion coefficient material is Zirconium Tungstate ($ZrW_2O_8$), a ceramic exhibiting a negative thermal expansion coefficient over a wide temperature range ($0 - 1050\ K$). [16] Table 4.2 lists possible materials to be used for a two-material package. [17]

| **Material** | **Linear expansion,°C$^{-1}$** |
|---|---|
| Aluminium | $22.9 \acute{} 10^{-6}$ |
| Nickel | $11.9 \acute{} 10^{-6}$ |
| Steel | $11.7 \acute{} 10^{-6}$ |
| Brass | $20 \acute{} 10^{-6}$ |
| Copper | $17 \acute{} 10^{-6}$ |
| Silver | $18 \acute{} 10^{-6}$ |
| PVC | $190 \acute{} 10^{-6}$ |
| Quartz | $0.5 \acute{} 10^{-6}$ |

**Table 4.2 – Linear thermal expansion coefficients for different materials**

In the following sections, a theoretical design and experimental results regarding a two-material packaged Bragg grating are presented.

The thermal response of the centre wavelength for an unpackaged Bragg grating is expressed by: [18]

$$D l_{BT} = l_B (1 + x) DT \tag{4.5}$$

where $\xi$ is the fibre thermo-optic coefficient and $DT$ the change in temperature. For normal silica single-mode fibre, the wavelength-temperature sensitivity for Bragg gratings at $1550\,nm$ is $a_f \approx 13\ pm/^oC$. [18]

Figure 4.14 is a basic diagram of the two-material package. Material 1 has a lower thermal expansion coefficient than material 2. The fibre Bragg grating is mounted under tension on material 2. The device counteracts the shift in centre wavelength that the Bragg grating experiences due to thermal fluctuations by applying a counteracting stress on the fibre. The wavelength-strain sensitivity of a normal single mode fibre Bragg grating at $1550\,nm$ is $r_f \approx 1.2\ pm/me$. [18]

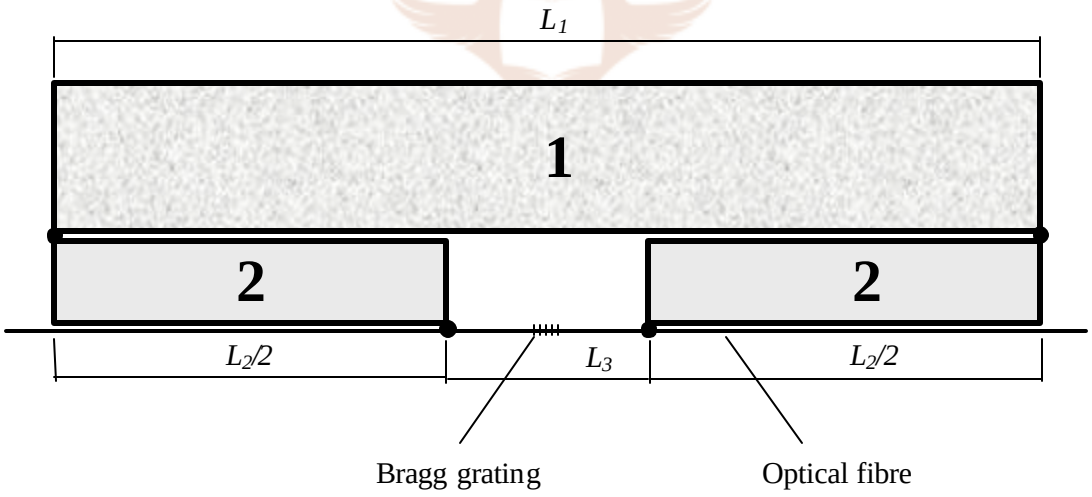


**Figure 4.14 – Two-material thermo-compensating package for a Bragg grating**

The thermal response for a two-material packaged Bragg grating is given by:

$$l_{BT} = l_B + \left(a_f DT + r_f e\right) \tag{4.6}$$

where $l_{BT}$ is the new centred wavelength, $a_f$ the thermal sensitivity of the Bragg grating, $r_f$ the strain sensitivity of the Bragg grating, $DT$ the change in temperature and $e$ the strain applied on the Bragg grating. Ideally $Dl_{BT} = l_{BT} - l_B$ must be zero. Therefore:

$$a_f DT = -r_f e \tag{4.7}$$

The lengths $L_1$, $L_2$ and $L_3$ are related to each other by:

$$L_3 = L_1 - L_2 \tag{4.8}$$

$$L_3' = L_1' - L_2' \tag{4.9}$$

where $L_1'$, $L_2'$ and $L_3'$ are the new lengths due to the thermal expansion of the materials. The strain applied on the grating due to the lengthening of the plates is:

$$e = \frac{L_3' - L_3}{L_1 - L_2} = \frac{\left(L_1' - L_2'\right) - L_3}{L_1 - L_2} \tag{4.10}$$

The change in length, which each plate exhibits, is governed by:

$$DL_{1,2} = a_{1,2} L_{1,2} DT \tag{4.11}$$

where $a_{1,2}$ is the linear thermal expansion coefficient and $DL_{1,2}$ the increase in length for each material. The new lengths for material 1 and material 2 are expressed by:

$$L_1' = a_1 L_1 DT + L_1 \tag{4.12}$$

$$L_2' = a_2 L_2 DT + L_2 \tag{4.13}$$

where $a_1$ and $a_2$ are the linear thermal expansion coefficients of materials 1 and 2 respectively. The change in the centred wavelength is given by:

$$D l_{BT} = a_f DT + \frac{DT r_f a_1 L_1}{L_1 - L_2} - \frac{DT r_f a_2 L_2}{L_1 - L_2} \tag{4.14}$$

with $L_1$ and $L_2$ related by:

$$\frac{L_2}{L_1} = \frac{a_f + a_1 r_f}{a_f + a_2 r_f} \tag{4.15}$$

Several variables govern the performance of the package. In order to design an optimum package, a sensitivity analysis in terms of the resultant centre wavelength shift for each variable is therefore necessary. The sensitivity of each variable is given by:

$$\frac{\partial\left(\frac{D l_{BT}}{DT}\right)}{\partial L_1} = \frac{r_f a_1}{L_1 - L_2} - \frac{r_f (a_1 L_1 - a_2 L_2)}{(L_1 - L_2)^2} \tag{4.16}$$

$$\frac{\partial\left(\frac{D l_{BT}}{DT}\right)}{\partial L_2} = -\frac{r_f a_2}{L_1 - L_2} + \frac{r_f (a_1 L_1 - a_2 L_2)}{(L_1 - L_2)^2} \tag{4.17}$$

$$\frac{\partial\left(\frac{D l_{BT}}{DT}\right)}{\partial a_1} = \frac{r_f L_1}{L_1 - L_2} \tag{4.18}$$

$$\frac{\partial\left(\frac{D l_{BT}}{DT}\right)}{\partial a_2} = -\frac{r_f L_2}{L_1 - L_2} \tag{4.19}$$

$$\frac{\partial\left(\frac{Dl_{BT}}{DT}\right)}{\partial a_f} = 1 \tag{4.20}$$

$$\frac{\partial\left(\frac{Dl_{BT}}{DT}\right)}{\partial r_f} = \frac{a_1 L_1 - a_2 L_2}{L_1 - L_2} \tag{4.21}$$

From Table 4.2, we selected nickel and aluminium for material 1 and material 2 respectively. A sensitivity analysis was performed and from the results, an optimum design could be made to package a *15 mm* Bragg grating. From Figure 4.15 (a) and Figure 4.15 (b) it is evident that as the lengths of $L_1$ and $L_2$ increases the sensitivity becomes less.

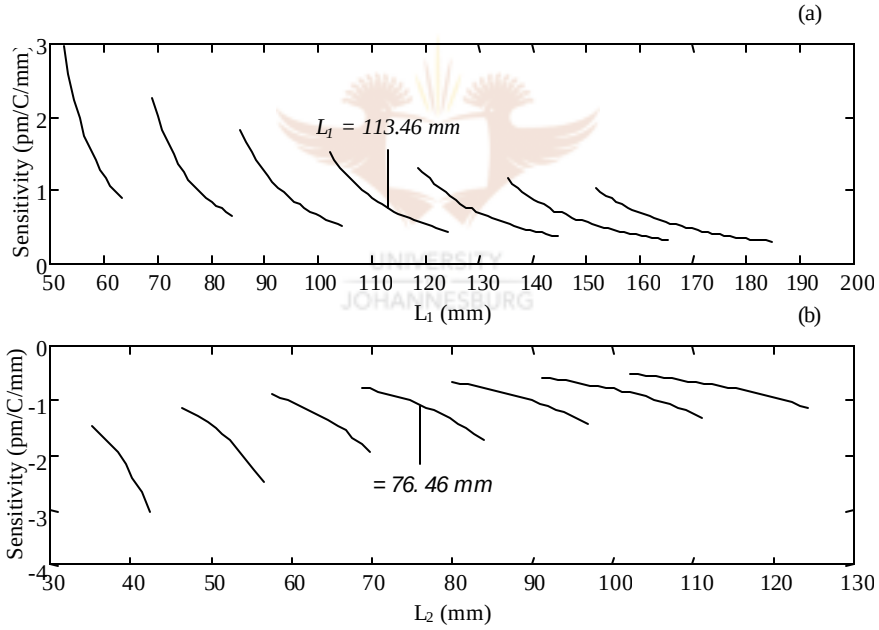


**Figure 4.15 – Sensitivity analysis for (a) $L_1$ (nickel) and (b) $L_2$ (aluminium)**

Table 4.3 summarizes the design parameters.

| Parameter | Value |
|---|---|
| $\alpha_1$ | $11.9 \times 10^{-6}/°C$ |
| $\alpha_2$ | $22.9 \times 10^{-6}/°C$ |
| $\alpha_f$ | $13\ pm/°C$ |
| $r_f$ | $1.2\ pm/me$ |
| $L_1$ | $113.46\ mm$ |
| $L_2$ | $76.46\ mm$ |
| $L_3$ | $37\ mm$ |

**Table 4.3 – Design parameters for the thermo-compensating package**

The *15 mm* DC- *apodized* Kaiser grating was packaged in a cylindrical package comprising a nickel tube ($L_1$) and an aluminium tube ($L_2$). A steel tip was used to cover the Nickel tube in order to secure the fibre. The error involved, using the steel is negligible because the linear thermal expansion coefficient of steel and nickel compares favourably (Table 4.2). It was estimated that in order to compensate over *100°C*, the fibre Bragg grating had to be pre-strained by *1083 me* before packaging. A Pratley Steel quickset epoxy was used to mount the two metal tubes and the fibre at the relevant positions.

The package was placed in a temperature-controlled oven and heated to determine the stability of the centre wavelength as a function of temperature. Figure 4.16 shows a relationship between the sensitivity of the centre wavelength versus temperature for the packaged Bragg grating. The dots indicate the experimental results the line is a straight-line approximation of the experimental results. From the data, it can be seen that the packaged Bragg grating exhibits an average wavelength-temperature sensitivity of 2.76 $pm/^oC$.

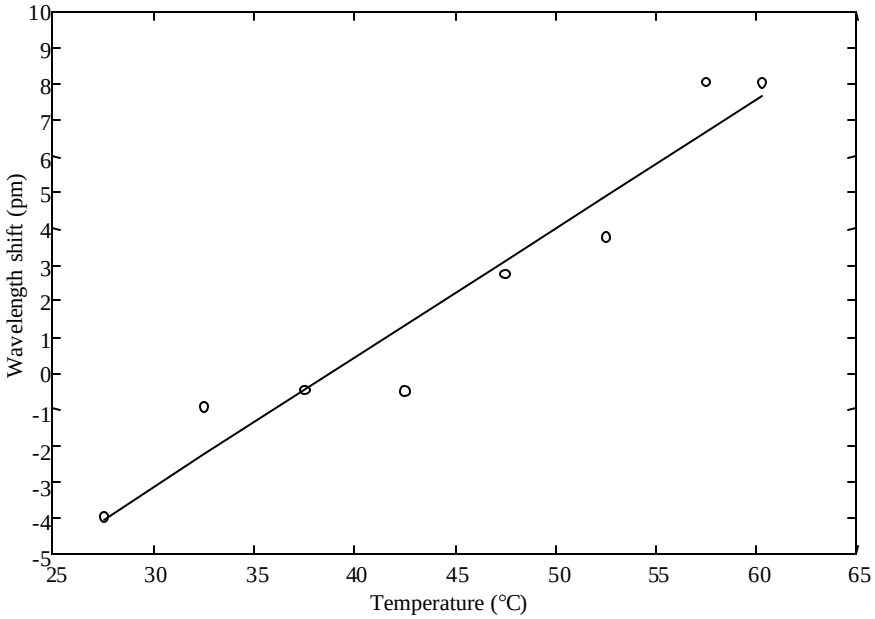


**Figure 4.16 – Centre wavelength stability for the thermo-compensated packaged Bragg grating**

The packaged Bragg grating exhibits a *0 pm/°C* stability near *38.8 °C*, indicating that the anticipated thermo response for the Bragg grating package was overcompensated for. This effect is due to an uncertainty in:

- The linear thermal expansion coefficient of the materials.
- The specific wavelength-temperature sensitivity of an uncompensated Bragg grating.
- The specific wavelength-strain sensitivity of an uncompensated Bragg grating.

## 4.5 CIRCULATOR AND BRAGG GRATING OADM

Figure 4.17 shows the experimental reflection spectrum of a *15 mm* DC-*apodized* Kaiser grating with a theoretical ac index change of $Dn(z) = 2.5 \times 10^{-4}$. The Bragg grating was UV-written by using a KrF (*248 nm*) excimer laser in the core of Boron-doped PS-1550 photosensitive fibre. The grating was prestrained by *200 me*, resulting in a shift of *1.63 nm* after relaxing the fibre. The grating exhibits a peak reflectance of *93.15 %*, an FWHM of *0.19 nm* and a channel isolation of *22.84 dB*. The

characteristic sidelobes are present due to a modulated index envelope. Ignoring the "stitching" errors, a channel isolation of *30 dB* is expected (spectrum: *1546.5 nm* to *1549.4 nm*).

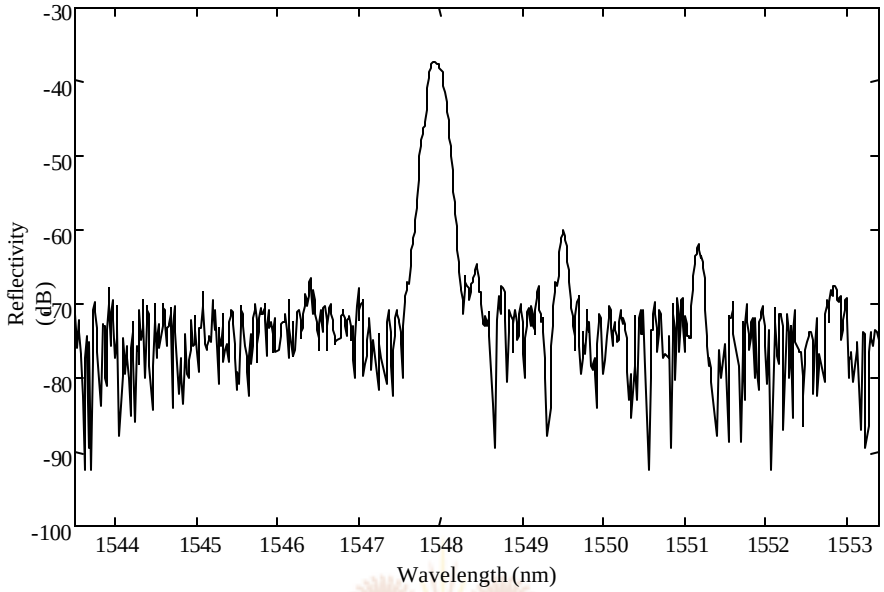


**Figure 4.17 – Experimental reflectivity for Bragg grating (Kaiser, $\Delta n(z) = 2.5 \times 10^{-4}$)**



The grating was combined with an E-TEK three-port circulator to perform the drop function of an OADM (Figure 4.18). A tunable laser diode source was used to sweep over a broad bandwidth (*1540 nm* to *1555 nm*) to test the transmission and drop capabilities of the device.

Figure 4.19 (a) shows the transmission spectrum at the through port and Figure 4.19 (b) the reflection spectrum at the drop port. The transmission spectrum shows a loss to radiation modes on the short wavelength side. This could be due to a tilt in the Bragg grating induced during the writing process, causing the Bragg grating to be blazed. [4] This would also explain the disappearance of the sidelobes on the shorter wavelength side, evident in the reflection spectrum (Figure 4.17).

The dropped channel shows an insertion loss of *1.84 dB*. This value can be decreased by ± *0.4 dB* if the splice-loss is kept to a minimum. By merely cascading another three-port circulator, the same Bragg grating can be used to realize an OADM to add and drop the channel.

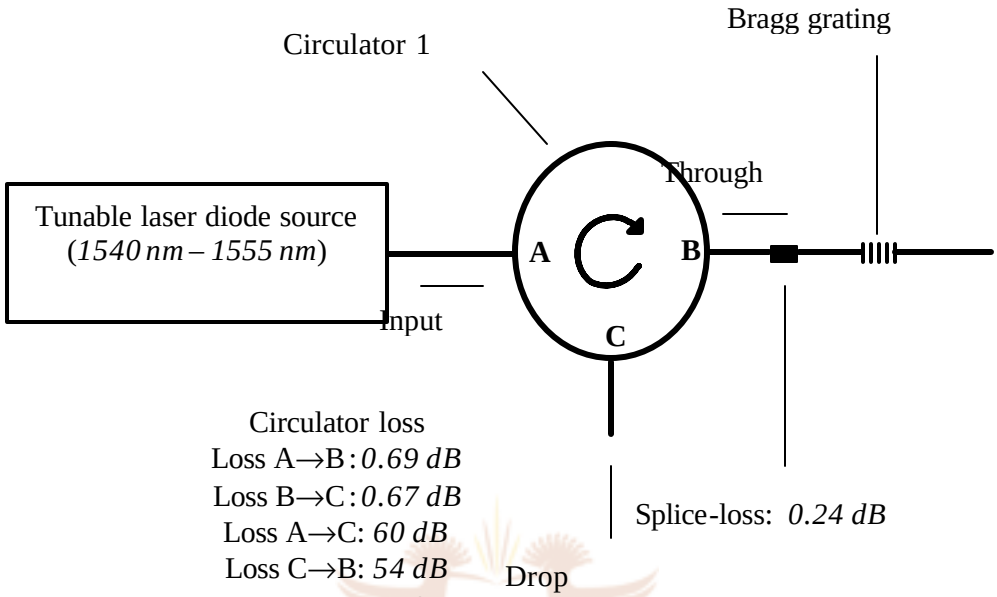


**Figure 4.18 – Experimental setup for the three-port circulator and Bragg grating**

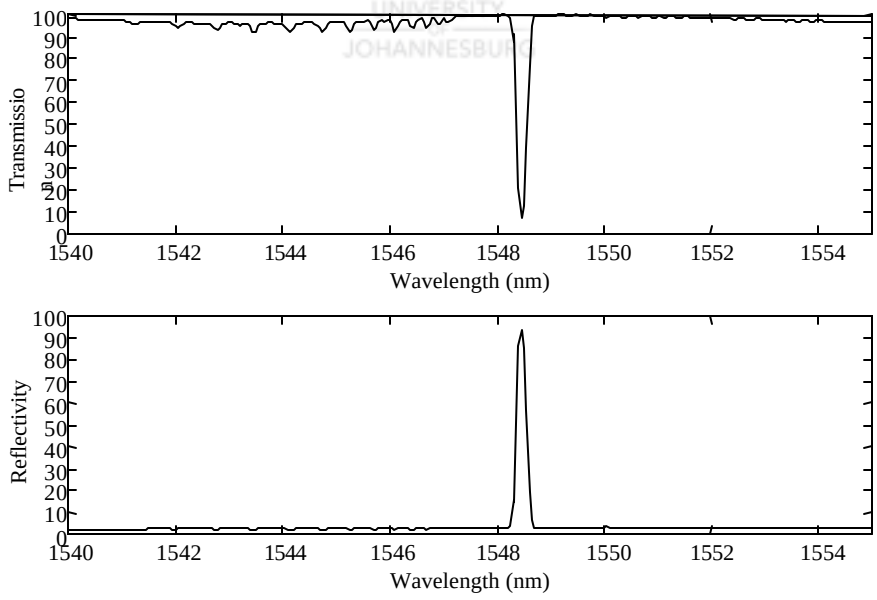


**Figure 4.19 – (a) Transmission spectrum at the through port and (b) the reflection spectrum at the drop port**

## 4.6 CONCLUSION

It was shown that different types of *apodization* profiles are available to optimize the filtering capabilities (sidelobe suppression) of fibre Bragg gratings. When writing the Bragg grating, special care must be taken so that the preconditioning is sufficient and the envelope is not modulated. The envelope modulation can be suppressed by using smaller increments when translating the UV beam across the grating.

The wavelength-temperature sensitivity of the thermo-compensated packaged Bragg grating can be reduced by determining the exact linear thermal expansion coefficient of the materials. Uncertainty in the wavelength-temperature sensitivity and wavelength-strain sensitivity for an uncompensated Bragg grating also results in undesirable wavelength-temperature sensitivities.

The circulator and Bragg grating OADM exhibit a channel isolation of *22.84 dB* with an insertion loss of *1.84 dB*. The Bragg grating has a maximum reflection of *93.15 %* and an FWHM of *0.19 nm*. These properties are far from ideal but can be improved by optimizing the manufacturing process. Higher induced index changes can rectify the low maximum reflection of the Bragg grating. Keeping the splice-loss to a minimum can reduce the insertion loss by ± *0.4 dB*.



## 4.7 REFERENCES

1. K.O. Hill, B. Malo, F. Bilodeau and D.C. Johnson, “Photosensitivity in optical fibers”, Annual Review Material Science, volume 23, pp. 125-157, (1993).
2. M. Douay, W.X. Xie, T. Taunay, P. Bernage, and P. Niay, “Densification Involved in the UV-Based Photosensitivity of Silica Glasses and Optical Fibres”, Journal of Lightwave Technology, volume 15, number 8, pp.1329-1342, (1997).
3. I. Bennion, J.A.R. Williams, L. Zhang and K. Sugden, “UV-written in-fibre Bragg gratings”, Optical and Quantum Electronics, volume 28, pp. 93-135, (1996).
4. K.O. Hill and G. Meltz, “Fiber Bragg Grating Technology Fundamentals and Overview”, Journal of Lightwave Technology, volume 15, number 8, pp. 1263-1276, (1997).

5. K.O. Hill, Y. Fujii, D.C. Johnson and B.S. Kawasaki, "Photosensitivity in optical fiber waveguides: Application to reflection filter fabrication", Applied Physics Letters, volume 32, number 10, pp. 647-649, (1978).
6. G. Meltz, W.W. Morey and W.H. Glenn, "Formation of Bragg gratings in optical fibres by a transverse holographic method", Optics Letters, volume 14, pp. 823-825, (1989).
7. D.K.W. Lam and B.K. Garside, "Characterization of single-mode optical fiber filters", Applied Optics, volume 20, number 3, pp. 440-445, (1981).
8. K.O. Hill, B. Malo, D.C. Johnson and J. Albert, "Bragg gratings fabricated in monomode photosensitive optical fiber by UV exposure through a phase mask", Applied Physics Letters, volume 62, number 10, pp. 1035-1037, (1993).
9. S.R. Baker, H.N. Rourke, N. Baker and D. Goodchild, "Thermal Decay of Fiber Bragg Gratings Written in Boron and Germanium Codoped Silica Fiber", Journal of Lightwave Technology, volume 15, number 8, pp. 1470-1477, (1997).
10. C.S. Burrus, "Computer-Based Exercises For Signal Processing Using Matlab", Prentice Hall International, pp. 83-89, (1994).
11. K. Ennser, M.N. Zervas and R.I. Laming, "Optimization of Apodized Linearly Chirped Fiber Gratings for Optical Communication", IEEE Journal of Quantum Electronics, volume 34, number 5, pp. 770-778, (1998).
12. P.Z. Peebles, "Probability, Random Variables, and Random Signal Principles", McGraw-Hill, Singapore, third edition, pp. 49, (1999).
13. B. Malo, S. Theriault, D.C. Johnson, F. Bilodeau, J. Albert and K.O. Hill, "Apodised in-fibre Bragg grating reflectors photoimprinted using a phase mask", Electronics Letters, volume 31, number 3, pp. 223-224, (1995).
14. C.R. Giles, "Lightwave Applications of Fiber Bragg Gratings", Journal of Lightwave Technology, volume 15, number 8, pp. 1391-1404, (1997).
15. I. Ota, T. Tsuda, A. Shinozaki, S. Yodo and T. Ota, "Development of optical fiber gratings for WDM systems", Furukawa Review, number 19, pp. 35-40, (2000).
16. http://www.esc.cam.ac.uk/astaff/dove/zrw2o8.html
17. L.H. van Vlack, "Materials For Engineering: Concept and Application", Addison-Wesley publishing, first edition, pp. 588, (1982).
18. Y.J. Rao, "In-fibre Bragg grating sensors", Measurement of Science and Technology, volume 8, pp. 355-375, (1997).